PCCP

PAPER

View Article Online
View Journal | View Issue

Check for updates

Cite this: *Phys. Chem. Chem. Phys.*, 2025, **27**, 15163

Received 5th May 2025,
Accepted 30th June 2025

DOI: 10.1039/d5cp01700a

rsc.li/pccp

The overlapping fragment approach for non-orthogonal configuration interaction with fragments†

C. Sousa, [a] X. Dong,[b] R. Broer,[c] T. P. Straatsma[bd] and C. de Graaf [*ef]

The non-orthogonal configuration interaction with fragments (NOCI-F) approach is extended opening the possibility to study intramolecular processes and materials with covalent or ionic lattices. So far, NOCI-F has been applied to study intermolecular energy and electron transfer employing ensembles of fragments that do not have atoms or bonds in common. The here presented approach divides the target system into two overlapping fragments that share one or more atoms and/or one or more bonds. After the construction of a collection of (multiconfigurational) fragment wave functions in a state specific optimization procedure, the fragment wave functions are combined to form many-electron basis functions for the non-orthogonal configuration interaction of the whole system. The orbitals in the overlapping fragment are defined by a corresponding orbital transformation of the fragment orbitals through a singular value decomposition. The overlapping fragments approach is first illustrated for a model system and then used to highlight some possible applications of NOCI with overlapping fragments. The results of excited state diffusion in transition metal oxide, intramolecular singlet fission and magnetic interactions in organic biradicals and ionic compounds are discussed.

1 Introduction

Intermolecular electron and energy transfer play an important role in many chemical processes such as singlet fission,[1] generation of reactive oxygen species through photocatalysis,[2] conduction in molecular crystals,[3,4] molecular electronics[5–7] and singlet and triplet excitation energy transfer in organic light emitting diodes (OLEDs),[8] to name a few examples. The magnetic ordering of the spin moments in molecular crystals containing organic radicals is also an interesting example where intermolecular interactions are fundamental.

Based on Fermi's golden rule, many models are being used to quantify the rates of the different transfer processes.[9] The electronic coupling between initial and final states can be estimated from Frontier molecular orbital models such as the one developed by Michl and co-workers,[1,10] the dimer projection method,[11] the analytic overlap method,[12] and its extension to machine-learning.[13] Next, these couplings can also be obtained from supramolecular total energy calculations, including unrestricted Hartree–Fock,[14,15] multi-configurational wave functions approaches,[16–19] ionization and electron affinity coupled cluster,[20] time-dependent density functional theory (TD-DFT), quasi-particle energy DFT,[21] and semi-empirical methods such as density matrix tight-binding.[22] Furthermore, computational approaches have been extensively applied that rely on diabatization procedures among which the generalized Mulliken–Hush method[23] is one of the reference methods. Mulliken–Hush is based on diabatization through diagonalization of the dipole moment operator, but other choices of operators can also be used.[24]

Diabatization schemes based on the locality of the orbitals find their origin in the proposal of Cederbaum and co-workers of block diagonalization of the Hamiltonian.[25] This has been implemented in constrained DFT,[26] fragment-orbital DFT,[27,28] projector operator DFT[29] and diabatization using absolute localized orbitals.[30]

Many of the above mentioned schemes aim at the calculation of the coupling between initial and final states in processes where electron or holes are transferred. Energy transfer can be captured in models such as the Frenkel–Davydov exciton

---

[a] Departament de Ciència de Materials i Química Física and Institut de Química Teòrica i Computacional, Universitat de Barcelona, 08028 Barcelona, Spain
[b] National Center for Computational Sciences, Oak Ridge National Laboratory, Oak Ridge, TN 37831-6373, USA
[c] Zernike Institute for Advanced Materials, University of Groningen, 9747 AG Groningen, The Netherlands
[d] Department of Chemistry and Biochemistry, University of Alabama, Tuscaloosa, AL 35487-0336, USA
[e] Departament de Química Física i Inorgànica, Universitat Rovira i Virgili, 43007 Tarragona, Spain. E-mail: coen.degraaf@urv.cat
[f] ICREA, Pg. Lluís Companys 23, Barcelona, Spain

† Electronic supplementary information (ESI) available. See DOI: **https://doi.org/10.1039/d5cp01700a**

model[31,32] and its *ab initio* implementation by Herbert *et al.*[33] Other widely used models are based on the so-called Dexter and Förster couplings[34,35] and the transition dipole coupling model derived from it.[36,37]

Non-orthogonal configuration interaction with fragments (NOCI-F)[38–40] is designed to study the electronic structure of systems containing discrete fragments found in molecular crystals or (self-assembled) stacks of molecules and can be used to calculate electronic couplings without making any *ad hoc* assumption about the character of the initial or final state. It can be applied to study both energy and electron or hole transport processes.

Starting with an ensemble of fragments, in most cases a collection of molecules, NOCI-F first optimizes a set of multiconfigurational wave functions for different electronic states of each member of the ensemble. Typically, these are complete active space self-consistent field wave functions, but they can be of any type. The state specific optimization of the fragment states ensures a full account of the orbital relaxation, which can have a large impact on the quality of the ensemble wave function when fragment states are considered whose dominant electronic configurations are different. Once all the fragment states are generated, NOCI-F constructs the many-electron basis functions (MEBFs) of the whole ensemble as anti-symmetrized spin-adapted product of the fragment wave functions. In this way, we obtain an optimal (diabatic) representation of the electronic states involved in the energy and/or charge transfer processes among the fragments in the ensemble.

This procedure is to some extent similar to the active space decomposition method of Parker,[41,42] with the major difference that NOCI-F uses different orbitals for different configurations. This implies that the MEBFs and their orbitals are mutually non-orthogonal, which requires an extra computational effort for the calculation of the Hamiltonian. The upside is that the resulting wave function is very compact (the number of MEBFs is typically on the order of ten) and yet fully accounts for non-dynamic correlation and orbital relaxation. Dynamic correlation effects can be included through the procedure described in ref. 40. Other fragment based approaches to calculate interactions between monomers are the symmetry adapted perturbation theory[43–45] and the decomposition analysis of Lin and Corminboeuf.[46] Furthermore, we mention the recently published local active space state interaction singles (LASSIS) of Hermes and co-workers as an interesting approach to partition a system in fragments.[47]

In the last few years, NOCI-F is applied to study intermolecular energy and electron transfer processes such as exciton diffusion, electron and hole mobility, transformation of an excited singlet state into two singlet-coupled triplet states on neighboring molecules, *etc.*[40,48–51] Here, we present an extension of the NOCI-F method to tackle materials that do not have a molecular crystal and to study of intramolecular processes. With this extension that is based on earlier single-configuration work of Stoyanova *et al.*,[52] NOCI-F can be used to study processes such as intramolecular (excited state) charge transfer, magnetic coupling and excited state dispersion in transition metal compounds, or electron and hole mobility in polymeric materials. In short, the applicability window of the NOCI-F approach is vastly extended.

2 The overlapping fragments approach

The overlapping fragment approach starts by dividing the target system in two parts as illustrated in Fig. 1 for an organic molecule (left), a dinuclear transition metal complex (middle) and an embedded cluster representing a small portion of an ionic three-dimensional lattice. The area where the two fragments overlap can consist of a single atom (the bridging oxygen in the right panel), or a group of atoms (the azido groups in the central panel). In its most basic form, this area only contains the covalent bond that connects the two fragments, as shown in the left panel. In the latter case, an extra hydrogen (or a convenient group) is added to saturate the dangling bond in each fragment. These extra atoms are being taken care of in a later stage of the procedure.

Once the two fragments of the system are properly defined, multiconfigurational wave functions are separately optimized for the relevant electronic states of each fragment. The list of non-orthogonal fragment states typically include the ground state of the fragment, local excited states, and in case charge transfer effects can be expected to play a role in the system under study, one also includes cationic and anionic fragment states in the procedure. The so obtained fragment wave functions include the most important static electron correlation and a full orbital relaxation, that is, the orbitals in which the electronic states are expressed are optimally adapted to describe the respective states. Furthermore, the effect of dynamic correlation can be included by estimating the energy correction through multiconfigurational second-order perturbation theory approaches such as CASPT2 or NEVPT2. These correlation energy corrections on the fragment states are used later on in the procedure by shifting the diagonal matrix elements of the Hamiltonian of the full system as described in ref. 40.

The fragment states cannot be merged into MEBFs in the same way as is done in NOCI-F studies with ensembles of molecules that do not share atoms or bonds. In those cases, the MEBFs are directly constructed as anti-symmetrized spin-adapted products of the fragment wave functions. Now, additional steps need to be carried out to take into account the common part of the two fragments. To avoid the double

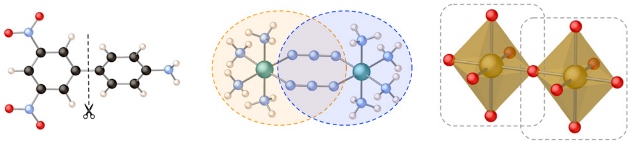

Fig. 1 Examples of systems that can be studied with the overlapping fragments approach. From left to right: 3′,5′-dinitro-[1,1′-biphenyl]-4-amine, a dinuclear Ni^{2+}-$(\mu\text{-}N_3^-)_2$ complex and a Cu_2O_{11} cluster cut from the La_2CuO_4 crystal.

counting of the electrons and nuclei in the overlapping part, not only electrons and nuclei need to be removed but also the set of orbitals of the whole system obtained by superimposing the orbitals of the two fragments must be reduced. However, the natural orbitals of the fragments have typically a rather delocalized character, and hence, it is impossible to unambiguously identify orbitals as belonging to the overlapping part of the system. This identification can efficiently be done by performing a corresponding orbital transformation of the orbitals of the two fragments. First, the overlap matrix ($\mathbf{S}_{\mathrm{MO}}^{\mathrm{AB}}$) of the occupied orbitals of the fragments A and B is constructed. In case of multiconfigurational fragment wave functions, the active orbitals are excluded to maintain the unitary character of the transformation. By performing a singular value decomposition (SVD) on the overlap matrix

$$\mathbf{S}_{\mathrm{MO}}^{\mathrm{AB}} = \mathbf{U}\lambda\mathbf{V}^{T} \quad (1)$$

pairs of orbitals of the two fragments are obtained that show maximal resemblance among them. Each transformed inactive orbital ψ_i of fragment A (defined by $\mathbf{U}$) has a non-zero overlap with at most one "corresponding" transformed inactive orbital ϕ_i in fragment B (defined by $\mathbf{V}$), and their overlap is given by the singular value λ_i. The corresponding orbitals with the largest overlap are identified as the orbitals that are localized on the part of the system where the fragments overlap and the in-phase combination of ψ and ϕ is kept, while the out-of-phase combination is eliminated from the set of orbitals. After this reduction of the orbital set, MEBFs of the whole system are formed by combining the CI wave functions of the fragment wave functions using the Clebsch–Gordan coefficients to ensure the spin symmetry.

The last step towards the final wave functions and energy is the actual non-orthogonal configuration interaction calculation on the whole system. The Hamiltonian and overlap matrix elements among the MEBFs constructed in the previous step are computed using the GNOME algorithm[53] implemented in the massively parallel and GPU-accelerated GronOR code.[39] Two thresholds have to be set, τ_{MO} and τ_{CI}. The first fixes the size of the common molecular orbital basis while the second controls the number of determinant pairs included in the construction of the NOCI matrix elements. The default values of 10^{-4} and 10^{-5} for τ_{MO} and τ_{CI} have been shown to give accurate results in previous applications of the NOCI-F approach.[40,48,49] Additionally, computational time can be saved by freezing the core orbitals, thus reducing the NOCI computation. The matrix elements give access to the electronic coupling between the states represented by the MEBFs and solving the eigenvalue problem results in NOCI energies and wave functions. The dynamic correlation energy correction can be applied in this stage of the procedure by transforming the Hamiltonian to an orthogonal MEBF basis, applying the correlation correction to the diagonal matrix elements and transforming back to the original non-orthogonal MEBFs. The shift applied is the sum of the correlation energy corrections of the fragment wave functions that constitute the MEBF. This neglects interfragment dynamic correlation, which is assumed to be small based on the understanding that dynamic electron correlation is short-ranged. The wall clock time of preparing the MEBFs from the (overlapping) fragment wave functions is negligible in comparison to the actual NOCI-F calculation, as it only involves an SVD and the construction of the CI expansion for each MEBF. The calculation of the Hamiltonian and overlap matrices spanned by the MEBFs requires an SVD, solving an eigenvalue problem and processing the list of two-electron integrals for each bra-ket determinant pair.[39,53]

3 OVLF at work

3.1 Aspartic acid from alanine and acetic acid

To illustrate the general procedure of the overlapping fragments approach, we first discuss the construction of aspartic acid from acetic acid and alanine, as depicted in Fig. 2. This has in itself no special interest, but highlights some of the essential aspects of the OVLF approach.

The ground state wave functions of acetic acid (fragment A) and alanine (fragment B) are optimized by the complete active space self-consistent filed (CASSCF) approach with an active space of two orbitals and two electrons for A, and 4 orbitals and 4 electrons for B. Fig. 3 and 4 contain the active orbitals and some of the inactive ones. Notice that the inactive orbitals are delocalized over the whole fragment and there is no way to isolate the electrons of the overlapping part. In this case the active orbitals are basically localized on the non-overlapping part of the fragments, only the second active orbital of acetic acid has a small amplitude on the hydrogen atoms of the CH_2 bridge. This is however not a problem, the active orbitals can extend into the overlapping region.

The overlap matrix of the natural orbitals of the two fragments is calculated in the geometry of the full system with a dummy hydrogen placed at the average position of two hydrogens that were introduced upon splitting the molecule in two (grey atoms in Fig. 2). Note that this is only necessary when extra atoms are required for a correct description of the fragments. For example, in case of embedded cluster calculations of ionic materials (see right panel of Fig. 1), the overlapping fragments approach can be employed without extra atoms.

The corresponding orbital transformation is performed in two parts. First, the deep core orbitals (C,N,O-1s) are transformed to localize the C-1s orbital of the overlapping CH_2 group, and subsequently, the corresponding orbitals are constructed for the remaining inactive orbitals. Using this two-step

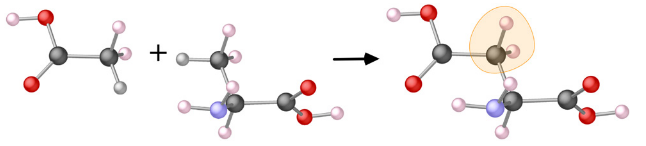
Fig. 2 Aspartic acid (right) constructed from the overlapping fragments acetic acid (left) and alanine (middle). The CH_2 group encircled in orange is common to both fragments. Note that each fragment has an extra hydrogen atom (marked in gray) to saturate the dangling bonds.

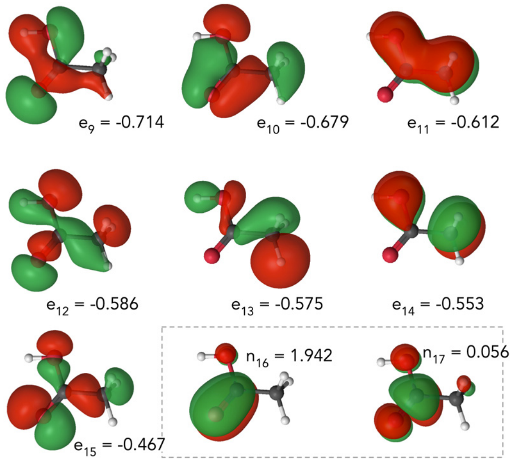

Fig. 3 Some inactive and the CASSCF(2,2) natural orbitals of acetic acid. e$_i$ and n$_i$ are the orbital energies and the natural occupation numbers of the inactive and active orbitals, respectively.

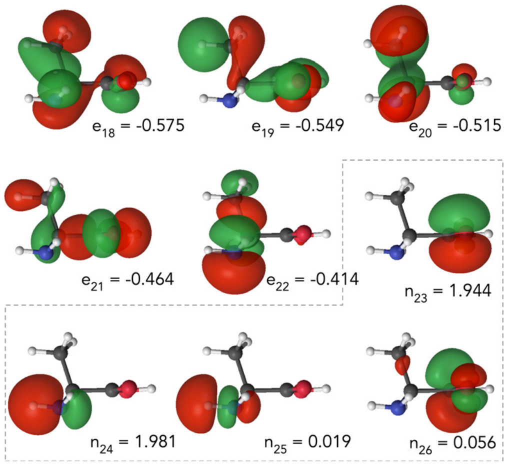

Fig. 4 Some inactive and the CASSCF(4,4) natural orbitals of alanine. e$_i$ and n$_i$ are the orbital energies and the natural occupation numbers of the inactive and active orbitals, respectively.

procedure, a well-defined set of core orbitals is maintained, which can be eliminated from the final NOCI calculation. The first two rows of Fig. 5 represent the five corresponding orbitals of acetic acid and alanine with the largest singular values. A sharp drop in the singular values is observed for the next pair of corresponding orbitals, $\lambda_6 = 0.039$. These orbitals (and the rest) do not show any contribution of the CH_2 group. As mentioned before, the in-phase combinations of the five corresponding orbital pairs are used to describe the CH_2 group of the full system, as can be seen in the last row of Fig. 5. These orbitals do no longer count with the basis functions of the dummy hydrogen atom and have been renormalized. The out-of phase combinations are removed and all other transformed orbitals are added to the set of molecular orbitals of the aspartic acid molecule after removing the basis functions of the dummy hydrogen atom and subsequent renormalization. At this point, the overlapping fragments approach can perform a Löwdin orthogonalization of the inactive orbitals, but this is optional.

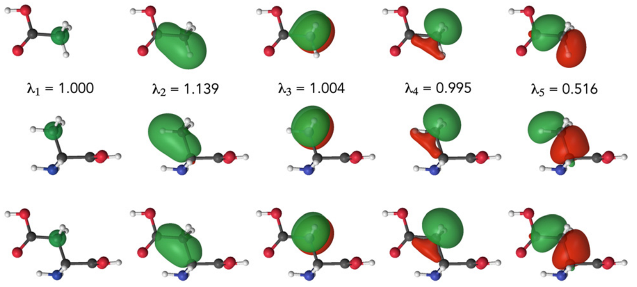

Fig. 5 From top to bottom: the five corresponding orbitals with the largest singular value λ_i of acetic acid, alanine and their in-phase combination in aspartic acid.

Table 1 compares the energies of several electronic structure approaches for the aspartic acid molecule. Fully optimizing the CASSCF(6,6) wave function provides the lowest energy. Excluding the fragment-to-fragment excitations in a general active space (GAS) SCF approach does not significantly increase the energy. The CASCI(6,6) with the molecular orbitals generated with the overlapping fragments approach described above give as expected a higher total energy. OpenMolcas[54] was used to calculate these energies. This program orthogonalizes the orbitals through the Gram-Schmidt approach, and hence, it is not surprising that the NOCI energy obtained with the Löwdin orthogonalized OVLF orbitals, NOCI(*ortho*), is practically the same. The only difference with the CASCI(6,6) is the fact that the NOCI active orbitals are not orthogonal to the inactive ones and that no fragment-to-fragment excitations are considered. Finally, the Table lists the NOCI energies obtained using the non-orthogonal orbitals. These lie approximately half-way the CASSCF and CASCI results. In the calculation with $\tau_{CI} = 10^{-6}$ only those bra-ket determinant pairs were considered in the evaluation of the NOCI energy whose absolute product of fragment CI coefficients is larger than 10^{-6}. This reduces the number of determinant pairs by a factor of 5.5, but does not significantly affect the final energy, in line with earlier studies of the NOCI-F approach for non-overlapping fragments. Although a single total ground state energy cannot provide a definite answer, the non-orthogonal OVLF orbitals seem to give a reasonable set of MOs to describe the molecules constructed from two overlapping fragments.

Table 1 Comparison of the total energies (in E_h) of aspartic acid. The CASCI and NOCI resuts have been obtained with orbitals from OVLF calculations

Method	Total energy
CASSCF(6,6)	−510.04063973
GASSCF(4,4;2,2)	−510.04060509
CASCI(6,6)	−509.86414831
NOCI (*ortho*)	−509.86421967
NOCI ($\tau_{CI} = 10^{-6}$)	−509.96299424
NOCI ($\tau_{CI} = 0$)	−509.96298675

3.2 Excited state dispersion in $CaFeO_3$

Electron and hole doping of ionic transition metal oxides can profoundly change the properties of these materials and lie at the basis of phenomena such as high-temperature superconductivity in the copper oxide perovskites.[55,56] Typically, theoretical studies make use of model Hamiltonians (t-J model, Hubbard Hamiltonian) to describe the effect of doping. The parameters of these models are either derived from experimental data or taken from computational studies. A common way of deriving the parameter that defines the mobility of the doped hole or electron by computation is by fitting the band structure with a tight binding expression for the dispersion $\varepsilon(k)$

$$\varepsilon(k) = \varepsilon_0 - 2t\cos(kx) \tag{2}$$

where t parametrizes the hole or electron mobility, k is the wave vector and x the length of the unit cell.[57,58] Band structures are normally obtained from density functional theory calculations, and hence, rely on an effective one-electron model for the electronic structure. Frontier molecular orbital approaches such as the DImer PROjection (DIPRO) method[11] are applied in the study of conduction properties of molecular crystals but are less useful for ionic (or covalent) lattices.

NOCI-F and NOCI-F with overlapping fragments can be used as alternative making use of many-electron functions contrary to the tight-binding and DIPRO parametrizations. Here, we report the hopping of an excess electron between two neighboring FeO_6 octahedra in $CaFeO_3$ as shown in Fig. 6. The electronic structure of the ground state has been analyzed by some of us ref. 59 and 60, showing that the electronic configurations arising from oxygen to iron excitations are dominant in the many-electron wave function. This results in an effective $3d^5$ configurations for Fe, in line with the regular (albeit tilted) octahedra in the crystal.

Since the FeO_6 octahedron is only slightly distorted, the electronic states in Table 2 are labeled by the symbols of the O_h symmetry group. The two components of the ^5E_g state are separated in energy by no more than 0.04 eV. Adding an extra electron to the FeO_6 octahedron lead to a sextet spin state of A_{1g} symmetry. The two fragments used in this study are the left and right FeO_6 octahedra of Fig. 6 with the central oxygen shared by both fragments.

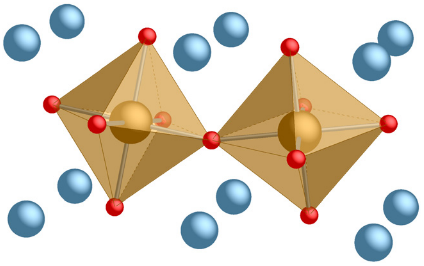

Fig. 6 Ball and stick representation of two neighboring octahedra in the *a*–*b* plane of the $CaFeO_3$ high temperature crystal phase.[61,62] Red spheres are oxygen, blue is calcium and the central gold-like spheres are iron.

Table 2 Hopping parameters of an excess electron in an embedded Fe_2O_{11} cluster representing the high temperature phase of $CaFeO_3$

Hopping	Doublet	Quartet	Sextet	Octet	Decaplet
$a^5E_g–^6A_{1g} \rightarrow {}^6A_{1g}–a^5E_g$	74.7	149.0	223.9	298.0	371.7
$a^5E_g–^6A_{1g} \rightarrow {}^6A_{1g}–b^5E_g$	124.8	250.2	375.8	498.4	621.5
$b^5E_g–^6A_{1g} \rightarrow {}^6A_{1g}–a^5E_g$	3.4	7.2	10.2	12.5	15.4
$b^5E_g–^6A_{1g} \rightarrow {}^6A_{1g}–b^5E_g$	16.3	33.4	50.0	64.8	80.8

With these three electronic states, there are four possible transfer pathways for the excess electron. The $^6A_{1g}$ state is either combined with the a^5E_g or b^5E_g state on the second fragment and electron transfer leads to one of the ^5E_g states on the first fragment combined with the symmetric sextet state on the second fragment. The two fragment spin states can be coupled to doublet, quartet, sextet, octet and decaplet and the results in the table show that the coupling between the initial and final states strongly depends on this spin coupling. In fact, these estimates follow very closely the Anderson and Hasegawa model for double exchange[63]

$$t(S) = \frac{1}{2}(2S+1)t_{\frac{1}{2}} \tag{3}$$

and the expression derived by Girerd for mixed-valence complexes[64]

$$E(S) = \pm t\frac{S+1/2}{S_{\max}+1/2} + \frac{1}{2}J(S_{\max}(S_{\max}+1) - S(S+1)) \tag{4}$$

for weak magnetic coupling between the two fragments ($J \ll t$). The slight distortion in the octahedron causes that the singly occupied e_g-like orbital of the a^5E_g state of the left fragment has its maximum extension along the axis that connect the two octahedra, whereas it is orthogonal to it for the other quintet state. The situation is inverted for the right fragment. This makes that the transfer of the excess electron involving a^5E_g (left) and b^5E_g (right) leads to the strongest coupling, while it approaches zero when the two E_g states are involved with e_g-like orbitals orthogonal to the Fe–O–Fe axis. Such analysis of the effect of orbital-ordering[65,66] is rather straightforward in the OVLF approach but more complicated when optimizing the wave function in a cluster containing the two octahedra because this cluster breaks the local symmetry of the Fe ions.

3.3 Intramolecular singlet fission

Intramolecular singlet fission has several advantages above the more traditional intermolecular process and has been actively studied over the last ten years. Early reports of intramolecular singlet fission were mainly concerned with semiconducting polymers,[67,68] but soon it was also reported in covalently linked acenes[69] and terrylenediimides.[70] Controlling the crystal packing in compounds with intermolecular singlet fission properties is a rather complex task, which can be steered to some extent by using different substituents on the core structure, but this is not a straightforward process. Covalently linked singlet fission chromophores provide more rigid structures and can give a larger control on the relative orientation of the singlet fission chromophores, for

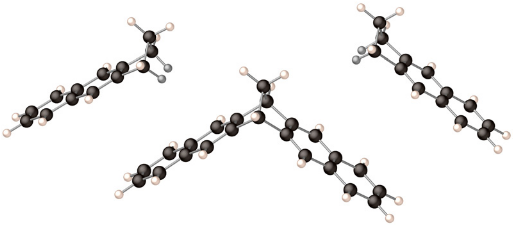

Fig. 7 Norbornyl-bridged naphthalene dimer (middle) with the two fragments on the left and right. Black spheres are carbon atoms, light spheres are hydrogens and the dark-grey spheres represent the hydrogens that are added to the fragments to saturate the covalent bonds that were broken upon splitting the molecule in two fragments.

example by using different linkers.[71–73] Although the structure of most polymers cannot be considered as rigid, the local structure is well-defined and combining donor and acceptor molecules in the chain can lead to polymers with interesting singlet fission properties.[74,75] Here, we describe how OVLF can be used to extract the electronic coupling between the initial excited singlet state and the singlet-coupled double triplet state in a norbornyl-bridged naphthalene dimer (see Fig. 7). This dimer is a model for the tetracene and pentacene analogues,[76,77] which have been studied in-depth.[78–80]

Table 3 reports the relative energies of the fragments states. Apart from the first excited singlet (S_1) and the lowest triplet state (T_1), it also reports the energies of the cationic (D^+) and the anionic (D^-) doublet states. These doublets are combined to form the MEBFs representing the charge transfer (CT) states. It is clear from the relative energies that this covalently-linked naphthalene dimer is not a real candidate for showing singlet fission as the energy of the singlet coupled double triplet MEBF has a relative energy that is more than 1 eV higher than the singlet excited MEBF. Note that the energy of the T_1T_1 MEBFs is about 0.25 eV lower than two times the energy of the fragment T_1 state, indicating a significant binding energy of the two triplet excitons.

The actual NOCI calculation (*i.e.*, solving the generalized eigenvalue problem defined by the NOCI Hamiltonian and overlap matrices) leads to six adiabatic states, whose energies and MEBF expansion coefficients are given in Table 4. The final NOCI wave functions show that the singlet exciton is delocalized over the two fragments with the in-phase combination slightly lower in energy than the out-of-phase combination. The coupling between the two local singlet excitons is 17 meV. The CT states show a similar delocalization over the two fragments, the coupling between the two CT MEBFs is 25 meV.

Table 3 CASSCF(6,6) and CASPT2 relative energies of the fragment states and NOCI-F relative energies of the MEBFs with correlation correction. All energies in eV

State	CASSCF	CASPT2	Ref. weight	MEBF	NOCI-F
S_0	0.00	0.00	0.620	S_0S_0	0.00
S_1	5.64	4.63	0.613	S_1S_0, S_0S_1	4.51
T_1	3.60	3.25	0.603	T_1T_1	6.27
D^+	7.17	7.71	0.620	D^+D^-, D^-D^+	5.42
D^-	2.41	1.06	0.610		

Table 4 NOCI-F relative energies (in eV) and wave function expansion of the norbornyl-brdiged naphthalene dimer

	NOCI-F wave functions					
	Ψ_1	Ψ_2	Ψ_3	Ψ_4	Ψ_5	Ψ_6
ΔE	0.00	4.48	4.52	5.40	5.46	6.27
S_0S_0	−1.000	0.000	−0.011	−0.001	−0.003	−0.002
S_1S_0	0.016	−0.733	−0.680	0.005	0.002	−0.002
S_0S_1	−0.016	−0.680	0.733	0.000	0.005	0.002
T_1T_1	0.001	0.000	0.003	0.002	−0.010	−1.000
D^+D^-	−0.002	0.006	0.001	0.761	0.649	−0.006
D^-D^+	0.001	−0.002	0.003	0.649	−0.761	0.010

Finally, we mention that the coupling between the S_1S_0–S_0S_1 and the T_1T_1 MEBFs is 5.3 meV. This coupling includes the effect of the CT states, and corresponds to the so-called CT-enhanced coupling. Unlike many other cases, this coupling is almost identical to the direct coupling due to the very weak interaction of the singlet excitonic state and the double triplet state with the CT states, on the order of 5 meV. These interactions were calculated to be one or two orders of magnitude larger in previous studies on crystalline tetracene and pentacene, causing a significant enhancement of the singlet fission couplings when CT states were taken into account. We expect a similar effect in these norbornyl-bridged dimers for the larger acenes, which are currently under study.

3.4 Magnetic interactions

The NOCI-F method can potentially be applied to study magnetic interactions between two fragments that can either be molecules, magnetic metal centers, or portions of a molecule. In fact, the method has been successfully applied to the study of the magnetic coupling between pairs of organic radicals in molecular crystals.[40] This study showed the ability of the NOCI-F method not only to quantitatively describe magnetic interactions, but also to provide a straightforward interpretation of the different contributions to the magnetic coupling. However, to achieve good accuracy, the threshold on the product of the CI coefficients considered to construct the NOCI Hamiltonian, τ_{CI}, has to be set at 10^{-7}, tighter than the usual value of 10^{-5} applied when dealing with electron transfer processes. This is due to the small magnitude of the energy differences between different magnetic states. The goal here is to extend this study to other magnetic systems where the fragments are no longer molecules, but rather parts of a molecule or ionic metal centered clusters. Two different types of magnetic systems will be analyzed. First, two organic biradical molecules, where the magnetic interaction can be rationalized as arising from two radical molecular fragments, and, second, an ionic transition metal oxide, where the interaction between two neighbor metal centers is studied by splitting the system into two ionic single metal clusters with their respective coordination sphere.

The magnetic coupling strength between the two fragments, A and B, J_{AB}, is estimated from the isotropic Heisenberg Hamiltonian

$$\hat{H} = -J_{AB}\hat{S}_A\cdot\hat{S}_B \tag{5}$$

in terms of energy differences between the spin states resulting from the different couplings of the local spin moments of the two interacting fragments, $\hat{S}_A$ and $\hat{S}_B$.

3.4.1 Organic biradicals. Ullman's biradicals are a wide family of magnetic molecules based on nitronylnitroxide radicals connected by a large variety of couplers.[81,82] The simplest member of this family consists of two nitronylnitroxide radicals directly bounded, *i.e.* without any linker (see Fig. 8). The structure of this biradical has been characterized by X-ray experiments[83] showing a twist angle of ~55° between the two nitronylnitroxide units and a D_2 point group symmetry. Magnetic susceptibility measurements[83] reveal an antiferromagnetic coupling with a singlet–triplet energy gap of -311 cm^{-1}. The magnetic properties of this compound have been extensively studied by theoretical methods, and it has been shown that the interaction cannot be described by the usual representation of one unpaired electron per radical.[84] Instead, the radical fragments are only properly described when considering three active electrons, with the spin density mainly localized on the NO groups and the central carbon atom.

In order to apply the NOCI-F method, the biradical molecule at the experimental geometry is divided in two nitronylnitroxide radical fragments with the dangling bond of the central C atom saturated by a H atom at a distance of 1.05 Å. This extra H atom will be removed when superimposing the two fragments. To ensure a correct description of the fragment wave function, a CAS(3,3) including 3π orbitals and 3 electrons has been considered. For each radical, six electronic states have been computed: the doublet ground state, D_0, two anionic states in which the nitronylnitroxide radical wins one electron that can be coupled either to a singlet, S^-, or a triplet state, T^-, the two equivalent cationic states, with one electron less in the active space, S^+ and T^+, and a quartet state, Q_0, corresponding to the maximum spin multiplicity of the radical. The energy of the singlet and triplet states have been computed by NOCI calculations in two ways. First, as a direct singlet or triplet coupling between the D_0 states of each radical, constructing the corresponding D_0D_0 MEBF. Alternatively, the non-orthogonal Hamiltonian is increased by taking into account the charge transfer states between the two radicals. That leads to a 5 × 5 Hamiltonian including the D_0D_0, S^-S^+, S^+S^-, T^-T^+ and T^+T^- MEBFs for the singlet state and a 9 × 9 Hamiltonian based on the D_0D_0, S^-T^+, T^+S^-, T^-S^+, S^+T^-, T^-T^+, T^+T^-, Q_0D_0, D_0Q_0 MEBFs for the triplet state.

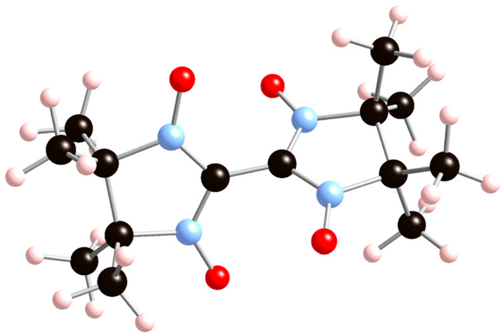

Fig. 8 Ball and stick representation of the simplest Ullman's biradical. Dark spheres are carbon atoms, blue is nitrogen, red is oxygen and light spheres represent hydrogen.

Table 5 NOCI-F magnetic coupling parameter J (in cm^{-1}) for the Ullman biradical for different thresholds on the size of the common molecular orbitals basis set, τ_{MO}. τ_{CI} is fixed to 10^{-7}. In the frozen core calculations the 1s core orbitals are not included in the NOCI

τ_{MO}	10^{-5}	10^{-6}	10^{-7}
GS only	−175	−165	−159
GS + CT	−185	−176	−170
+ DCEC	−191	−182	−176
Frozen core			
GS only	−229	−181	−155
GS + CT	−242	−195	−169
+ DCEC	−249	−201	−175

The values of the magnetic coupling, J, for the Ullman biradical, computed as the energy difference between the singlet and triplet states, are disclosed in Table 5. Various values of the common molecular orbital basis set threshold, τ_{MO}, have been considered, ranging from 10^{-5} to 10^{-7}. Computing the singlet and triplet states from the direct D_0D_0 coupling (GS only in Table 5) leads to an antiferromagnetic coupling (negative J value) which slightly decreases when tightening the τ_{MO} threshold. Including the charge transfer states between the two fragments (see entry GS + CT in Table 5) increases the value of J by around 10–11 cm^{-1}, meaning that for this particular system, charge transfer effects do not play an important role. The effect of the remaining dynamic electron correlation on the magnetic coupling has been considered by shifting the diagonal matrix elements by a dynamic correlation energy correction (DCEC).[40] This correction has been computed by CASPT2 calculations, using the standard zeroth-order Hamiltonian (with an IPEA shift of 0.25 a.u.), on all the fragment states. Including the effect of the dynamical electron correlation only increases the J value by 6 cm^{-1}, see +DCEC results in Table 5. This is in accordance with previous results by Angeli *et al.*,[84] pointing out that for the magnetic coupling of the Ullman's biradical, dynamic electron correlation only plays a minor role.

In order to discern the effect in the magnetic coupling of freezing the core orbitals, similar calculations have been performed now freezing the 1s core orbitals of all C, N and O atoms. Results are collected in the lower part of Table 5. It can be observed that the frozen core approach leads to larger absolute values of J, specially for a τ_{MO} of 10^{-5}. Strengthening the τ_{MO} threshold decreases the J values in a way that both, frozen core and no frozen, practically coincide for a τ_{MO} threshold of 10^{-7}. In the frozen core NOCI-F calculations, as found when considering all the orbitals, both the charge transfer and dynamical electron correlation effects are small. The magnitude of the magnetic coupling obtained by these calculations, -176 cm^{-1}, is quite far from the experimentally measured value of -311 cm^{-1}. Here it is important to note that the system is divided in two fragments by the C–C bond that connects the two radicals. In both fragments, this bond is modeled by a simpler C–H bond. This relatively simple approach to split the molecule into two fragments results in a crude a representation of the connection. Given that in the biradical systems like this one the magnetic coupling occurs mainly due to a through-bond coupling, it is not completely unexpected to recover only part of the coupling. Other possibilities of defining the overlapping fragments are being explored at present. A promising approach is to saturate each fragment with a CH_3 group instead of a mere hydrogen atom. In this way the central C–C bond is much better described and magnetic couplings calculated through the fragments approach are likely to increase.

A second aspect that has been analyzed is the influence of the distance of the saturating H atom to the central C of the radical fragment. From the initial distance of 1.05 Å, a somewhat larger, 1.15 Å, and shorter, 0.95 Å, distances have been considered. Results reported in Table 6 show very small changes in the magnitude of the magnetic coupling, of 8 cm^{-1}, when varying the distance by 0.2 Å. Again, the small effect of the inclusion of charge transfer and dynamic electron correlation effects for this particular system becomes evident.

A second example of magnetic interactions in biradicals is given in Table 7. This concerns the interaction between the spin moments on the NO groups bridged by a phenyl group as shown in Fig. 9. The interaction leads to antiferromagnetic coupling when the second NO group is in the *para* position (left) and ferromagnetic coupling for the *meta* position (middle). The fragments are phenyl nitroxides (right), which are overlapping through the phenyl group. Previous computational studies on these biradicals estimated the couplings to be around −2000 cm^{-1} for the *para* compound and near +700 cm^{-1} for the molecule with the nitroxides in *meta*.,[85] being the latter in good agreement with experimental estimates.[86] To the best of our knowledge, there are no experimental estimates for the *para* molecule.

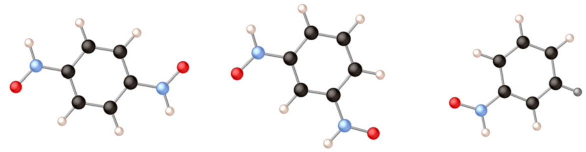

Fig. 9 Ball and stick representations of *para* (left) and *meta* (middle) phenylene dinitroxide, and the phenylene nitroxide fragment (right). Black is carbon, light blue is nitrogen, red is oxygen, the small spheres are hydrogens. The darker small sphere represents the hydrogen that is added to saturate the bond that was broken.

The following fragment states were considered: the doublet ground and first excited states (D_0 and D_1), the singlet and triplet cationic states (S^+ and T^+) and the singlet and triplet anionic states (S^- and T^-). These states were combined in three types of MEBFs for the NOCI: first, the ground state (GS) of the phenylene dinitroxides (D_0D_0); second, the local excited states (LE, D_1D_0 and D_0D_1); and third, the charge transfer states (CT). For the singlet state of the whole molecule we consider S^+S^-, S^-S^+ T^+T^- and T^-T^+ and for the triplet state, we include the S^+T^-, S^-T^+, T^+S^-, T^+T^-, T^-S^+, and T^-T^+ CT states.

Table 6 NOCI-F magnetic coupling parameter J (in cm^{-1}) for the Ullman biradical for different fragment carbon–hydrogen distances (in Å). τ_{MO} and τ_{CI} have been set to 10^{-5} and 10^{-7}, respectively

d(C–H)	0.95	1.05	1.15
GS only	−179	−175	−171
GS + CT	−194	−185	−187
+ DCEC	−197	−191	−189

Table 7 NOCI-F magnetic coupling parameter J (in cm^{-1}) for *meta*- and *para* phenylene-bridged nitroxide biradicals

	Meta	*Para*
GS only	70	−181
GS + LE	73	−181
GS + CT	264	−792
All states	269	−969

Only considering the neutral doublet states of the two fragments, the character of the coupling is correctly reproduced, although the strength of the coupling is significantly underestimated. Adding the local excited doublet states does not change the coupling, while including the charge transfer states in the NOCI calculation strongly increases the coupling between the two spin moments. The final estimates based on a NOCI among the GS, LE and CT states results in a moderate coupling of around −1000 cm^{-1} for *para*-perylene dinitroxide and 270 cm^{-1} for the *meta* variant, corresponding to an underestimation of the coupling by approximately a factor of two, similar to what is observed in the study of Ullman's biradical as commented before in this section.

3.4.2 Ionic compounds. In addition to the above mentioned role of electron and hole doping, interactions between localized spin moments in strongly correlated materials are also essential ingredients for the many intriguing phenomena that have been observed for these extended systems. The most basic, and often strongest interaction is the isotropic interaction of the spin moments between nearest neighbors giving rise to ordered phases of ferromagnetic or antiferromagnetic nature. As test system for the NOCI-F with overlapping fragments, we report the results of the magnetic coupling between two Ni^{2+} ions in NiO. The shortest distance between Ni atoms in the fcc crystal is 2.95 Å, but these ions are only weakly coupled being linked through oxygen at an angle of 90°.[87] Instead, we consider the interaction along the linear Ni–O–Ni link for which the nickels are separated by 4.17 Å. Using the same definition of the Heisenberg Hamiltonian as in the previous section, this coupling is characterized by J = −20 meV, antiferromagnetic in nature.[88]

Ab initio calculations based on a wave function approach and with density functional theory were both able to reproduce the experimental coupling with reasonable precision.[89–91] NOCI calculations for the magnetic coupling in these materials have also been reported. The study of van Oosten *et al.* in a series of copper oxides revealed the importance of incorporating charge

Table 8 NOCI-F magnetic coupling parameters J (in meV) for the 180° Ni–O–Ni links in NiO

	J_{ST}	J_{TQ}
GS only	−0.2	−0.2
GS + NH	−0.5	−0.1
GS + NH + CT	−4.4	−4.7
+ DCEC	−7.8	−8.2

transfer states expressed in their own optimal set of orbitals in the description of the electronic structure.[92,93] The separate optimization of charge transfer states is much more complicated in systems with larger magnetic moments. The larger number of unpaired electrons translates in the presence of several electronic states arising from transitions within the partially filled TM-3d shell intercalated between the magnetic ground state and the target charge transfer states. The procedure for obtaining a state specific description as described in ref. 94 and 95 could be applied but are extremely tedious and not very practical for routine application. Other algorithms such as root selection based on overlap are not always successful, often the character of the target state is lost during the optimization process. It is in this line that the NOCI-F with overlapping fragments may be useful to construct charge transfer states (and other relevant electronic states) and estimate the coupling through the NOCI approach applied previously for the cuprates.

Table 8 summarizes the NOCI results considering different collections of singlet, triplet and quintet states of an embedded Ni_2O_{11} cluster. The wave functions of the Ni_2O_{11} cluster are obtained by superimposing the wave functions of the NiO_6 fragments, similar to the study on $CaFeO_3$ of Section 3.2. The fragment states that were considered are the $^3A_{2g}$ ground state, the ^2E_g states with one electron less and one electron more to construct the CT states and the lowest excited singlet state ^1E_g. The latter, so-called non-Hund state, is not considered in the Heisenberg Hamiltonian and was demonstrated to be responsible for deviations in the regular energy splitting of the different spin states predicted by the Heisenberg Hamiltonian.[96,97]

Only considering the ground state wave functions of the fragments leads to three virtually degenerate spin states. The addition of the non-Hund (NH) states does not change the picture drastically, only a small deviation to the regular splitting is observed. A more important increase in the coupling is observed when the CT states are included in the NOCI calculation and applying the dynamic correlation energy correction for the fragment states further increases the coupling. Unfortunately, the final result of ~ -8 meV only reproduces 50% of the experimental coupling, similar to what was observed for the Ullman biradical.

4 Computational information

The cluster models used in the study of the excited state dispersion in $CaFeO_3$ are embedded in a layer of Fe and Ca *ab initio* embedding potentials[98] derived in the previous study of the electronic structure of $CaFeO_3$.[59,60] The Madelung potential in the cluster region is accurately represented by a set of optimized point charges. The basis set is taken from the ANO-RCC library[99] of OpenMolcas with a contraction scheme of (6s 5p 3d 1f) for Fe and (4s 3p 1d) for oxygen, the same as in ref. 59 and 60. The molecular orbitals in the norbornyl-bridged naphthalene dimer are also expanded in the ANO-RCC basis set. Being a test application of OVLF, a relatively small contracted basis was used: C (3s 2p 1d) and H (2s 1p). To describe the C, N and O atoms of the Ullman's biradical and the phenylene dinitroxides the same ANO-RCC basis set was used as in the *ab initio* study reported in ref. 84 and 85. The contraction scheme for C, N and O is (5s 4p 2d 1f), while for H a (3s 2p 1d) contracted basis set has been used.

5 Conclusions and summary

Non-orthogonal configuration interaction with fragments (NOCI-F) is specifically designed to study energy and electron transfer processes. Multiconfigurational fragment wave functions are optimized in a state specific approach to account for orbital relaxation (different orbitals for different electronic configurations) and the static electron correlation. The fragment wave functions are combined as anti-symmetrized spin-adapted products to construct the many-electron basis functions for the NOCI of the whole system. Dynamic electron correlation effects can be included following the procedure described in ref. 40. This approach has been applied to study singlet fission in acenes and perylene diimides, exciton dispersion and magnetic coupling organic radicals.[40,48–50] However, the method in its original formulation is restricted to ensembles of fragments that do not share atoms and/or bonds, excluding intramolecular processes and materials with covalent or ionic lattices. To extend the applicability range of the NOCI-F approach, we have presented the overlapping fragments variant of NOCI-F. The system is divided in two fragments that share at least one atom or bond. The procedure is basically identical to the standard NOCI-F approach, but for the corresponding orbital transformation of the inactive fragment orbitals. This transformation identifies the inactive orbitals that are present in both fragments, enabling the elimination of one of them to avoid double counting.

Among the several applications that can be envisaged, we have first studied the electron transfer in the ionic $CaFeO_3$ lattice. The NOCI-F results closely follow the predictions of the Anderson–Hasegawa model[63] and the expression for double exchange derived by Girerd.[64] A clear advantage of the overlapping fragment approach is the fact that the fragments can be defined such that the site symmetry of the lattice is reproduced, which is generally not possible when the wave functions are directly optimized for a two-center cluster containing the metal centers involved in the electron transfer. The use of fragments with the correct site symmetry makes it possible to study effects such as orbital ordering, essential in many materials, for example the series of doped manganites $La_{1-x}Ca_xMnO_3$.[100]

The method is of course not restricted to the here studied electron transfer, it can also be used to calculate the diffusion of electronically excited states and the mobility of hole states, among other many-electron processes. By calculating the electronic coupling between initial and final states in different crystal directions, a many-electron band structure can be calculated as explained in ref. 51.

Whereas intermolecular singlet fission has been studied rather intensively, intramolecular singlet fission has important advantages. Choosing wisely the linker between the two parts of the molecule where the singlet exciton transforms into a singlet-coupled double triplet state can increase the singlet fission coupling significantly, or favor the triplet separation process. The here presented OVLF approach lies the foundations for the NOCI study of these processes, which is currently in progress. As proof-of-principle, we have studied the singlet fission in the norbornyl-bridged naphthalene dimer. The coupling in this covalently linked dimer is somewhat on the weak side, but is expected to be significantly larger in systems with larger acenes, used in experimental studies.

The underestimation of the magnetic coupling parameters observed for the organic biradicals and the transition metal oxide studied here can for a large part be ascribed to shortcomings in the description of the region that connects the two fragments. For these systems, the through-bond interactions are dominant compared to the through-space interactions, while the opposite holds for the molecular materials containing organic radicals studied in ref. 40. In the latter case, NOCI-F predicts very precisely the magnetic coupling parameters.

In Ullman's biradical, the central C–C bond originates from the corresponding orbital transformation mostly involving the two C–H orbitals of the fragments. The possibility of using a methyl group to saturate the broken bond is currently under investigation. For the other two systems, the situation is somewhat different. The two fragments do share the group that connects the two magnetic centers; in NiO the central oxygen of the Ni_2O_{11} cluster, and the phenyl group in the phenylene dinitroxides. Their role in the magnetic coupling is however rather passive, the active orbitals of the fragments are basically localized on the magnetic center and extend very little onto the part of the systems that connects them. An improvement can possibly be obtained by defining a third fragment containing the connecting atoms. Fragment states should be constructed for this fragment with the orbitals that play a role in connecting the magnetic centers in the active space. These active orbitals, the π-orbitals of the phenylene group and the O-$2p_\sigma$ orbital for the Ni_2O_{11} cluster, would then also be considered in the MEBF construction following the multi fragment approach[101] implemented in GronOR.

Notice that the energy differences that play a role in the determination of the magnetic coupling strength are very small and that small deviations in the description of the coupling of the two fragments can have a substantial effect on the coupling. This effect is less dramatic for other applications of the OVLF approach.

A possible application of NOCI with overlapping fragments that has not been considered here is the intramolecular charge transfer, either thermally induced[102] or after populating electronically excited states.[103] In both cases, there are no major methodological problems to apply the OVLF approach and extract the electronic coupling of initial and final states of the electron transfer process.

The overlapping fragments approach is not restricted to systems that can be divided in two fragments, but can also applied to systems with more fragments. For example, in an ABCD supersystem one can first account for the interaction between subsystems A and B with C and D treated as spectators. Next, fragment B and C are coupled and finally C is coupled to D. The total NOCI matrices of the ABCD systems are then constructed from the Hamiltonian and overlap matrices of the three dimer fragments. This can of course be generalized to trimers (ABC with D as spectator and BCD with A as spectator) if second neighbour interactions are expected to be important.

Conflicts of interest

There are no conflicts to declare.

Data availability

The computer codes used in the present study are freely available for the gitlab repository at **https://gitlab.com/gronor/gronor**.

Acknowledgements

Financial support was provided by the Ministry of Science and Innovation of the Spanish administration through the projects PID2021-126076NB-I00, PID2023-148238NB-I00, and Maria de Maetzu CEX2021-001202-M and by the Generalitat de Catalunya through the projects 2021SGR00079 and 2021SGR00110. This work used resources of the Oak Ridge Leadership Computing Facility (OLCF) at the Oak Ridge National Laboratory, which is supported by the Office of Science of the U.S. Department of Energy (DOE) under Contract DE-AC05-00OR22725 through the INCITE Project CHM154 and SummitPLUS Project CHM198. Part of the calculations were performed on Leonardo@CINECA (Italy) within the EuroHPC-JU programme. This manuscript has been authored in part by UT-Battelle, LLC, under contract DE-AC05-00OR22725 with the US Department of Energy (DOE). The US government retains and the publisher, by accepting the article for publication, acknowledges that the US government retains a nonexclusive, paid-up, irrevocable, worldwide license to publish or reproduce the published form of this manuscript, or allow others to do so, for US government purposes. DOE will provide public access to these results of federally sponsored research in accordance with the DOE Public Access Plan (**https://energy.gov/downloads/doe-public-access-plan**).

Notes and references

1 M. B. Smith and J. Michl, *Chem. Rev.*, 2010, **110**, 6891–6936.

2 Y. Nosaka and A. Y. Nosaka, *Chem. Rev.*, 2017, **117**, 11302–11336.

3 P. Gómez, J. Cerdá, M. Más-Montoya, S. Georgakopoulos, I. da Silva, A. Garca, E. Ort, J. Aragó and D. Curiel, *J. Mater. Chem. C*, 2021, **9**, 10819–10829.

4 A. Farokhi, H. Shahroosvand, G. Delle Monache, M. Pilkington and M. K. Nazeeruddin, *Chem. Soc. Rev.*, 2022, **51**, 5974–6064.

5 V. P. Georgiev and J. E. McGrady, *J. Am. Chem. Soc.*, 2011, **133**, 12590–12599.

6 D. Xiang, X. Wang, C. Jia, T. Lee and X. Guo, *Chem. Rev.*, 2016, **116**, 4318–4440.

7 H. Oberhofer, K. Reuter and J. Blumberger, *Chem. Rev.*, 2017, **117**, 10319–10357.

8 F. Li, A. J. Gillett, Q. Gu, J. Ding, Z. Chen, T. J. H. Hele, W. K. Myers, R. H. Friend and E. W. Evans, *Nat. Commun.*, 2022, **13**, 2744.

9 C.-P. Hsu, *Acc. Chem. Res.*, 2009, **42**, 509–518.

10 E. A. Buchanan, Z. Havlas and J. Michl, *Adv. Quantum Chem.*, 2017, **75**, 175–227.

11 B. Baumeier, J. Kirkpatrick and D. Andrienko, *Phys. Chem. Chem. Phys.*, 2010, **12**, 11103–11113.

12 O. G. Ziogos and J. Blumberger, *J. Chem. Phys.*, 2021, **155**, 244110.

13 R. Hafizi, J. Elsner and J. Blumberger, *J. Chem. Theory Comput.*, 2023, **19**, 4232–4242.

14 J. Logan and M. D. Newton, *J. Chem. Phys.*, 1983, **78**, 4086–4091.

15 C. J. Calzado and J. F. Sanz, *J. Am. Chem. Soc.*, 1998, **120**, 1051–1061.

16 C. J. Calzado and J.-P. Malrieu, *Phys. Rev. B: Condens. Matter Mater. Phys.*, 2001, **63**, 214520.

17 Z. Tabookht, X. López, C. de Graaf, N. Guihéry, N. Suaud and N. Ben Amor, *J. Comput. Chem.*, 2012, **33**, 1748–1761.

18 A. Kubas, F. Hoffmann, A. Heck, H. Oberhofer, M. Elstner and J. Blumberger, *J. Chem. Phys.*, 2014, **140**, 104105.

19 O. G. Ziogos, A. Kubas, Z. Futera, W. Xie, M. Elstner and J. Blumberger, *J. Chem. Phys.*, 2021, **155**, 234115.

20 C.-H. Yang and C.-P. Hsu, *J. Chem. Phys.*, 2006, **124**, 244507.

21 K.-Y. Kuan, S.-H. Yeh, W. Yang and C.-P. Hsu, *J. Phys. Chem. Lett.*, 2024, **15**, 6126–6136.

22 J. T. Kohn, N. Gildemeister, S. Grimme, D. Fazzi and A. Hansen, *J. Chem. Phys.*, 2023, **159**, 144106.

23 R. J. Cave and M. D. Newton, *Chem. Phys. Lett.*, 1996, **249**, 15–19.

24 Y. Shu, Z. Varga, S. Kanchanakungwankul, L. Zhang and D. G. Truhlar, *J. Phys. Chem. A*, 2022, **126**, 992–1018.

25 T. Pacher, L. S. Cederbaum and H. Köppel, *J. Chem. Phys.*, 1988, **89**, 7367–7381.

26 T. Van Voorhis, T. Kowalczyk, B. Kaduk, L. Wang, C.-L. Cheng and Q. Wu, *Annu. Rev. Phys. Chem.*, 2010, **61**, 149–170.

27 K. Senthilkumar, F. C. Grozema, F. M. Bickelhaupt and L. D. A. Siebbeles, *J. Chem. Phys.*, 2003, **119**, 9809–9817.

28 S. Sen, B. Senjean and L. Visscher, *J. Chem. Phys.*, 2023, **158**, 054115.

29 S. Ghan, C. Kunkel, K. Reuter and H. Oberhofer, *J. Chem. Theory Comput.*, 2020, **16**, 7431–7443.

30 Y. Mao, A. Montoya-Castillo and T. E. Markland, *J. Chem. Phys.*, 2019, **151**, 164114.

31 J. Frenkel, *Phys. Rev.*, 1931, **37**, 17–44.

32 A. S. Davydov, *Sov. Phys.*, 1964, **18**, 496–499.

33 A. F. Morrison, Z.-Q. You and J. M. Herbert, *J. Chem. Theory Comput.*, 2014, **10**, 5366–5376.

34 D. L. Dexter, *J. Chem. Phys.*, 1953, **21**, 836–850.

35 T. Förster, *Discuss. Faraday Soc.*, 1959, **27**, 7–17.

36 W. H. Moore and S. Krimm, *Proc. Natl. Acad. Sci. U. S. A.*, 1975, **72**, 4933–4935.

37 T. L. C. Jansen, *J. Chem. Phys.*, 2021, **155**, 170901.

38 R. K. Kathir, C. de Graaf, R. Broer and R. W. A. Havenith, *J. Chem. Theory Comput.*, 2020, **16**, 2941–2951.

39 T. P. Straatsma, R. Broer, A. Sánchez-Mansilla, C. Sousa and C. de Graaf, *J. Chem. Theory Comput.*, 2022, **18**, 3549–3565.

40 A. Sánchez-Mansilla, C. Sousa, R. K. Kathir, R. Broer, T. P. Straatsma and C. de Graaf, *Phys. Chem. Chem. Phys.*, 2022, **24**, 11931–11944.

41 S. M. Parker, T. Seideman, M. A. Ratner and T. Shiozaki, *J. Chem. Phys.*, 2013, **139**, 021108.

42 I. Kim, S. M. Parker and T. Shiozaki, *J. Chem. Theory Comput.*, 2015, **11**, 3636–3642.

43 B. Jeziorski, R. Moszynski and K. Szalewicz, *Chem. Rev.*, 1994, **94**, 1887–1930.

44 L. N. Anderson, F. W. Aquino, A. E. Raeber, X. Chen and B. M. Wong, *J. Chem. Theory Comput.*, 2018, **14**, 180–190.

45 J. Garcia, R. Podeszwa and K. Szalewicz, *J. Chem. Phys.*, 2020, **152**, 184109.

46 K. H. Lin and C. Corminboeuf, *J. Phys. Chem. A*, 2020, **124**, 10624–10634.

47 M. R. Hermes, B. Jangid, V. Agarawal and L. Gagliardi, *J. Chem. Theory Comput.*, 2025, DOI: **10.1021/acs.jctc.5c00387**.

48 C. Sousa, A. Sánchez-Mansilla, R. Broer, T. P. Straatsma and C. de Graaf, *J. Phys. Chem. A*, 2023, **127**, 9944–9958.

49 X. López, T. P. Straatsma, A. Sánchez-Mansilla and C. de Graaf, *J. Phys. Chem. C*, 2023, **127**, 16249–16258.

50 C. Sousa, X. Lopez, X. Dong, R. Broer, T. P. Straatsma and C. de Graaf, *J. Phys. Chem. C*, 2025, **129**, 4290–4302.

51 A. Sánchez-Mansilla, I.-O. Stan, R. Broer and C. de Graaf, *J. Phys. Chem. C*, 2025, **129**, 2797–2812.

52 A. Stoyanova, C. Sousa, C. de Graaf and R. Broer, *Int. J. Quantum Chem.*, 2006, **106**, 2444–2457.

53 R. Broer and W. C. Nieuwpoort, *Theor. Chim. Acta*, 1988, **73**, 405–418.

54 G. Li Manni, I. F. Galván, A. Alavi, F. Aleotti, F. Aquilante, J. Autschbach, D. Avagliano, A. Baiardi, J. J. Bao, S. Battaglia, L. Birnoschi, A. Blanco-González, S. I. Bokarev, R. Broer, R. Cacciari, P. B. Calio, R. K. Carlson, R. C. Couto, L. Cerdán, L. F. Chibotaru, N. F. Chilton, J. R. Church, I. Conti, S. Coriani, J. Cuéllar-Zuquin,

R. E. Daoud, N. Dattani, P. Decleva, C. de Graaf, M. Delcey, L. De Vico, W. Dobrautz, S. S. Dong, R. Feng, N. Ferré, M. Filatov, L. Gagliardi, M. Garavelli, L. González, Y. Guan, M. Guo, M. R. Hennefarth, M. R. Hermes, C. E. Hoyer, M. Huix-Rotllant, V. K. Jaiswal, A. Kaiser, D. S. Kaliakin, M. Khamesian, D. S. King, V. Kochetov, M. Krosnicki, A. A. Kumaar, E. D. Larsson, S. Lehtola, M. B. Lepetit, H. Lischka, P. López Ros, M. Lundberg, D. Ma, S. Mai, P. Marquetand, I. C. D. Merritt, F. Montorsi, M. Mörchen, A. Nenov, V. H. A. Nguyen, Y. Nishimoto, M. S. Oakley, M. Olivucci, M. Oppel, D. Padula, R. Pandharkar, Q. M. Phung, F. Plasser, G. Raggi, E. Rebolini, M. Reiher, I. Rivalta, D. Roca-Sanjuán, T. Romig, A. A. Safari, A. Sánchez-Mansilla, A. M. Sand, I. Schapiro, T. R. Scott, J. Segarra-Mart, F. Segatta, D.-C. Sergentu, P. Sharma, R. Shepard, Y. Shu, J. K. Staab, T. P. Straatsma, L. K. Sørensen, B. N. C. Tenorio, D. G. Truhlar, L. Ungur, M. Vacher, V. Veryazov, T. A. Voß, O. Weser, D. Wu, X. Yang, D. Yarkony, C. Zhou, J. P. Zobel and R. Lindh, *J. Chem. Theory Comput.*, 2023, **19**, 6933–6991.

55 A. P. Armitage, P. Fournier and R. L. Greene, *Rev. Mod. Phys.*, 2010, **82**, 2421–2487.

56 P. A. Lee, N. Nagaosa and X.-G. Wen, *Rev. Mod. Phys.*, 2006, **78**, 17–85.

57 H. Rosner, H. Eschrig, R. Hayn, S.-L. Drechsler and J. Málek, *Phys. Rev. B: Condens. Matter Mater. Phys.*, 1997, **56**, 3402–3412.

58 R. Weht and W. E. Pickett, *Phys. Rev. Lett.*, 1998, **81**, 2502–2505.

59 A. Sadoc, C. de Graaf and R. Broer, *Phys. Rev. B: Condens. Matter Mater. Phys.*, 2007, **75**, 165116.

60 A. Sadoc, R. Broer and C. de Graaf, *J. Chem. Phys.*, 2007, **126**, 134709.

61 M. Takano, S. Nasu, T. Abe, K. Yamamoto, S. Endo, Y. Takeda and J. B. Goodenough, *Phys. Rev. Lett.*, 1991, **67**, 3267–3270.

62 P. M. Woodward, D. E. Cox, E. Moshopoulou, A. W. Sleight and S. Moritomo, *Phys. Rev. B: Condens. Matter Mater. Phys.*, 2000, **62**, 844–855.

63 P. W. Anderson and H. Hasegawa, *Phys. Rev.*, 1955, **100**, 675–681.

64 J.-J. Girerd, *J. Chem. Phys.*, 1983, **79**, 1766–1775.

65 B. Halperin and R. Englman, *Phys. Rev. B: Condens. Matter Mater. Phys.*, 1971, **3**, 1698–1708.

66 K. I. Kugel and D. I. Khomskii, *Sov. Phys. JETP*, 1973, **37**, 725–730.

67 A. J. Musser, M. Al-Hashimi, M. Maiuri, D. Brida, M. Heeney, G. Cerullo, R. H. Friend and J. Clark, *J. Am. Chem. Soc.*, 2013, **135**, 12747–12754.

68 E. Busby, J. Xia, Q. Wu, J. Z. Low, R. Song, J. R. Miller, X.-Y. Zhu, L. M. Campos and M. Y. Sfeir, *Nat. Mater.*, 2015, **14**, 426–433.

69 S. N. Sanders, E. Kumarasamy, A. B. Pun, M. T. Trinh, B. Choi, J. Xia, E. J. Taffet, J. Z. Low, J. R. Miller, X. Roy, X.-Y. Zhu, M. L. Steigerwald, M. Y. Sfeir and L. M. Campos, *J. Am. Chem. Soc.*, 2015, **137**, 8965–8972.

70 E. A. Margulies, C. E. Miller, Y. Wu, L. Ma, G. C. Schatz, R. M. Young and M. R. Wasielewski, *Nat. Chem.*, 2016, **8**, 1120–1125.

71 N. V. Korovina, J. Joy, X. Feng, C. Feltenberger, A. I. Krylov, S. E. Bradforth and M. E. Thompson, *J. Am. Chem. Soc.*, 2018, **140**, 10179–10190.

72 N. V. Korovina, N. F. Pompetti and J. C. Johnson, *J. Chem. Phys.*, 2020, **152**, 040904.

73 G. Yu, L. Yang, Y. Gao, Z. Guo, Y. Tiam, Y. Wang, Y. Wan, Y. Han, W. Yang, J. Song and X. Ma, *J. Phys. Chem. Lett.*, 2024, **15**, 12561–12570.

74 J. T. Blaskovits, M. Fumanal, S. Vela and C. Corminboeuf, *Chem. Mater.*, 2020, **32**, 6515–6524.

75 J. T. Blaskovits, M. Fumanal, S. Vela, R. Fabregat and C. Corminboeuf, *Chem. Mater.*, 2021, **33**, 2567–2575.

76 J. D. Cook, T. J. Carey and N. H. Damrauer, *J. Phys. Chem. A*, 2016, **120**, 4473–4481.

77 T. J. Carey, E. G. Miller, A. T. Gilligan, T. Sammakia and N. H. Damrauer, *Org. Lett.*, 2018, **29**, 457–460.

78 C. J. Imperiale, P. Green, E. G. Miller, N. H. Damrauer and M. W. B. Wilson, *J. Phys. Chem. Lett.*, 2019, **10**, 7463–7469.

79 A. T. Gilligan, E. G. Miller, T. Sammakia and N. H. Damrauer, *J. Am. Chem. Soc.*, 2019, **141**, 5961–5971.

80 R. D. Dill, K. E. Smyser, B. K. Rugg, N. H. Damrauer and J. D. Eaves, *Nat. Commun.*, 2023, **14**, 1180.

81 E. F. Ullman and D. G. B. Boocock, *J. Chem. Soc. D*, 1969, 1161.

82 E. F. Ullman, J. H. Osiecki, D. G. B. Boocock and R. Darcy, *J. Am. Chem. Soc.*, 1972, **94**, 7049–7059.

83 F. Alies, D. Luneau, J. Laugier and P. Rey, *J. Phys. Chem.*, 1993, **97**, 2922–2925.

84 C. Angeli, C. J. Calzado, C. de Graaf and R. Caballol, *Phys. Chem. Chem. Phys.*, 2011, **13**, 14617–14628.

85 C. J. Calzado, C. Angeli, C. de Graaf and R. Caballol, *Theor. Chem. Acc.*, 2011, **128**, 505–519.

86 T. Ishida and H. Iwamura, *J. Am. Chem. Soc.*, 1991, **113**, 4238–4241.

87 J. Kanamori, *J. Phys. Chem. Solids*, 1959, **10**, 87–98.

88 M. J. Massey, N. H. Chen, J. W. Allen and R. Merlin, *Phys. Rev. B: Condens. Matter Mater. Phys.*, 1990, **42**, 8776–8779.

89 C. de Graaf, F. Illas, R. Broer and W. C. Nieuwpoort, *J. Chem. Phys.*, 1997, **106**, 3287–3291.

90 C. de Graaf, C. Sousa, I. de, P. R. Moreira and F. Illas, *J. Phys. Chem. A*, 2001, **105**, 11371–11378.

91 D. Ködderitzsch, W. Hergert, W. M. Temmerman, Z. Szotek, A. Ernst and H. Winter, *Phys. Rev. B: Condens. Matter Mater. Phys.*, 2002, **66**, 064434.

92 A. B. van Oosten, R. Broer and W. C. Nieuwpoort, *Int. J. Quantum Chem.*, 1995, **56**, 241–243.

93 A. B. van Oosten, R. Broer and W. C. Nieuwpoort, *Chem. Phys. Lett.*, 1996, **257**, 207–212.

94 B. Meyer, A. Domingo, T. Krah and V. Robert, *Dalton Trans.*, 2014, **43**, 11209–11215.

95 A. Domingo, C. Angeli, C. de Graaf and V. Robert, *J. Comput. Chem.*, 2015, **36**, 861–869.

96 R. Bastardis, N. Guihéry and C. de Graaf, *Phys. Rev. B: Condens. Matter Mater. Phys.*, 2007, **76**, 132412.

97 R. Bastardis, N. Guihéry and C. de Graaf, *J. Chem. Phys.*, 2008, **129**, 104102.

98 Z. Barandiarán and L. Seijo, *J. Chem. Phys.*, 1988, **89**, 5739–5746.

99 B. O. Roos, R. Lindh, P.-Å. Malmqvist, V. Veryazov and P.-O. Widmark, *J. Phys. Chem. A*, 2005, **109**, 6575–6579.

100 A. Daoud-Aladine, J. Rodrguez-Carvajal, L. Pinsard-Gaudart, M. T. Fernández-Daz and A. Revcolevschi, *Phys. Rev. Lett.*, 2002, **89**, 097205.

101 A. Sánchez-Mansilla, PhD thesis, Universitat Rovira i Virgili, 2024.

102 E. Evangelio, M.-L. Bonnet, M. Cabañas, M. Nakano, J.-P. Sutter, A. Dei, V. Robert and D. Ruiz-Molina, *Chem. – Eur. J.*, 2010, **16**, 6666–6677.

103 M. Fujitsuka, S. S. Kim, C. Lu, S. Tojo and T. Majima, *J. Phys. Chem. B*, 2015, **119**, 7275–7282.